NUMERICAL AND EXPERIMENTAL INVESTIGATION OF THERMAL PRETREATMENT FOR LITHIUM-ION BATTERY RECYCLING

E. E. BARROS DE SOUZA [*†], C. SPIJKER [†], Z. RAONIC [†] AND D. C. MAXIM [†]

[*] K1-MET GmbH, Austria
COMET Module FuLIBatteR
Stahlstraße 14, 4020 Linz, Austria
e-mail: emerson@k1-met.com, www.k1-met.com

[†] Chair of Thermal Processing Technology (TPT)
Technical University of Leoben
Franz Josef-Straße 18, 8700 Leoben, Austria
email: tpt@unileoben.ac.at, www.tpt-unileoben.at

Key words: Lithium-ion battery, Recycling, Pretreatment, CFD-DEM.

Abstract. Conventional recycling of lithium-ion batteries (LIBs) generally proceeds through stages of discharging, dismantling, shredding, and thermal treatment. The pyrolysis step is particularly important for removing organic components, such as electrolytes and binders. The present study focuses on investigating a thermal pretreatment process that integrates the discharging, dismantling, and pyrolysis steps. The process involves exposing LIB cells to moderate temperatures (below 300 °C) to trigger thermal runaway, while conserving the materials to be recycled. This method is intended to serve as an initial step in the LIB recycling chain, aiming to enhance the efficiency of downstream recycling processes, including pyro-, hydro-, and bio-metallurgy. To study this process, experimental and numerical approaches are being employed, with the goal of better understanding of the physical and chemical phenomena involved and providing insights for industrial optimization.

1 INTRODUCTION

Lithium-ion batteries (LIBs) are extensively studied for their applications in electronic products, electric vehicles (EVs), and energy storage devices. They are highly favored due to key properties, including lithium's high energy density, low self-discharge rate, and lack of memory effect [1]. Given that the service life of EV batteries typically ranges between five and eight years, the number of spent batteries is expected to increase significantly as current EVs become obsolete [2], with global end-of-life EV battery capacity projected to reach 174 GWh by 2030, surpassing the total installed EV battery capacity of 136.3 GWh in 2020 [3]. Motivated by carbon neutrality goals, the European Union has introduced regulations requiring target collection rates for portable batteries and light means of transport (LMT) batteries [4], with lithium recovery rates set to rise from 50% in 2027 to 80% by 2031. Furthermore, predictions indicate a significant increase in demand for battery cathode materials, particularly lithium, with supply estimated to reach 1,000 tons by 2030, while demand is expected to soar to

approximately 2,750 tons, potentially leading to significant deficits in these elements [3].

The use of lithium-ion batteries (LIBs) is important for achieving carbon neutrality in energy storage, ensuring a sustainable and climate-neutral transport system, and supporting the energy transition [5]. To meet the rising energy demand, aside from increasing energy production, the recycling efficiency must also rise to achieve a closed loop in the energy production and reuse cycle. Establishing large-scale recycling and securing the necessary raw materials are key to meeting this demand. Thermal pretreatment serves as a crucial pre-processing step for both pyro- and hydrometallurgical recycling of black mass. This approach induces a controlled thermal runaway, reaching up to 500°C, which safely deactivates the batteries. Specifically, this temperature range is ideal for volatilizing organic components (binders and electrolytes) [6, 7], which enhances the black mass quality and positively impacts downstream processing [8]. Furthermore, it is low enough to prevent the metallic foils from reaching their melting point [9].

The research is divided into two components: experimental and simulation. The experimental component involves replicating battery thermal deactivation in the laboratory to collect process-relevant data, including temperature distribution, off-gas evolution, and mass loss, during the thermal deactivation process. The simulation component uses experimental data to develop a thermal deactivation model concept. This concept is based on a CFD-DEM approach, where the transport phenomena between the batteries and the fluid phase are modeled using the Discrete Element Method (DEM) for the particulate phase and Computational Fluid Dynamics (CFD) for the continuous gaseous phase. This numerical approach is initially being used to confirm the reproducibility of thermal deactivation physics. In the future, it will be utilized as a tool to explore both the applicability and optimization of large-scale industrial designs for thermal deactivation processes.

2 METHODOLOGY

2.1 Thermal Deactivation Experiments

To investigate the thermal deactivation process, laboratory-scale experiments were conducted under controlled temperature conditions. The setup schematic is shown in Figure 1.

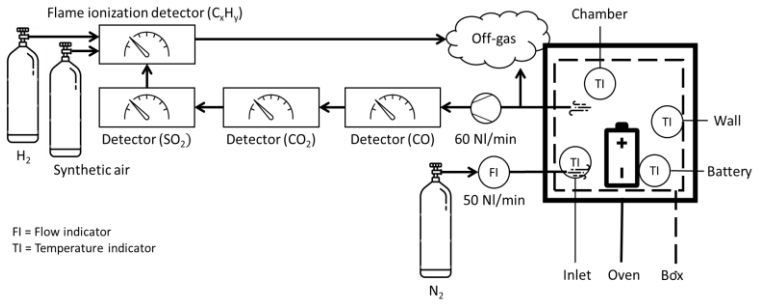

Figure 1: Simplified flow chart of the box test experiment

The experiment was designed to characterize the individual process steps for the thermal deactivation, so that the required data for the CFD-DEM model can be obtained. The procedure begins by measuring the battery initial mass, after which the cell is placed inside a steel box

with dimensions of 185 mm x 185 mm x 165 mm (length x width x height). Four thermocouples are attached at specific locations: the battery surface, the steel box wall, the chamber, and the nitrogen inlet gas line. The box is then properly sealed and placed into a laboratory muffle oven with the inlet and outlet gases pipes attached. The inlet line continuously purges preheated nitrogen gas at a flow rate of 50 Nl/min, providing a shielding atmosphere and forced convection. The outlet line is plugged with a pumping system, which directs the off gases to a series of gas analyzers to quantify the concentration of specific chemical species which are: CO, CO_2, SO_2 and C_xH_y. The oven is set to heat at a controlled rate of 9 °C/min. The slow rate is chosen to ensure the thermal runaway phenomenon is observed in a safe, reproducible way and that all events are properly detected by the instruments. The oven set point temperature is capped at 300 °C and held until the experiment's conclusion. The battery builds its temperature until it enters a two-stage process of thermal runaway. First, as the cell temperature rises, SEI (solid electrolyte interface) decomposition occurs, initiating the first stage of off gas release via the cell safety valve, which is detected by analyzers. Subsequently, further temperature increases accelerate degradation, leading to a larger quantity of off-gases, ignition, and eventual combustion, lead by the internal short circuits between electrodes, between current collectors and between the anode and the collector [10]. The experiment concludes after the cell temperature cools down and equalizes with the oven temperature. Finally, the steel box is removed, unsealed, and the cell is collected, re-measured, and stored. Figure 2 illustrates sample state before and after the experiment.

Figure 2: State of the battery sample before (left side) and after the experiment (right side)

On Figure 2 left side, the initial setup is visible. The intact cell sample is placed inside the steel box. Three of the four thermocouple wires are visible, routed to their specific locations: one on the inner wall of the box, one hanging in the chamber space, and one attached to the battery surface. The right side displays the final state of the sample after the experiment, placed inside a plastic container. One can observe the destruction of the original battery case. The remnants primarily consist of black mass powder (the mixture of active material remnants) and shredded, scattered metallic foils (aluminum and copper), confirming the severe degradation and material release caused by the thermal runaway event.

2.2 Thermal deactivation modeling

The thermal deactivation process was modeled using the CFD-DEM framework. The

possibility of representing a battery cell as a non-spherical body, including heat transfer and chemical reactions, coupled with gas fluid flow solver gives this approach an interesting novel characteristic in terms of numerical simulation of batteries. The open-source simulation software used was OpenFOAM® [11] for the CFD, LIGGGHTS® [12] for DEM, and the CFDEMcoupling® [13] package to combine both software packages. In this setup, the CFD side calculates the gas-phase dynamics (Eulerian phase), while the DEM side calculates the battery particle heat transfer, and thermal runaway (Lagrangian phase). The CFDEMcoupling facilitates the exchange of interaction variables between LIGGGHTS and OpenFOAM, ensuring accurate representation of gas–solid interactions throughout the simulation, and extends the physics with its own sub-models. Figure 3 shows an example of simulation loop. The DEM begins with sample preparation and uses the contact detection algorithm to calculate particle forces and solve the equations of motion. Next, data exchange transfers the relevant particle information to the CFD, where the porosity is updated. The CFD then solves the fluid equations and transfers the relevant forces back to the DEM. These forces are then considered at the new time step in the DEM side and the loop restarts.

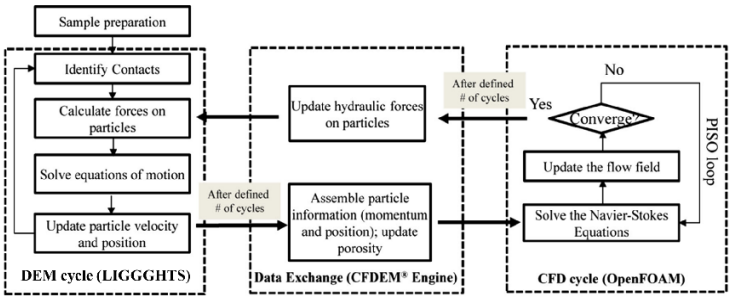

Figure 3: Simplified flowchart showing the DEM, CFD and CFDEMcoupling simulation process cycles [14]

2.2.1 Governing equations – Gas phase in presence of particles

The mass conservation for the gas phase is described by Equation (1) [15]:

$$\frac{\partial(\alpha_f \rho_f)}{\partial t} + \nabla \cdot \alpha_f \rho_f \mathbf{u}_f = S_\rho \tag{1}$$

where α_f represents the fluid void fraction, ρ_f is the fluid density, and $\mathbf{u}_f$ is the fluid velocity vector. S_ρ on the right-hand side represents the thermal runaway mass source. The momentum conservation for the gas phase is given by Equation (2) [13]:

$$\frac{\partial(\alpha_f \rho_f \mathbf{u}_f)}{\partial t} + \nabla \cdot \alpha_f \rho_f \mathbf{u}_f \mathbf{u}_f = -\alpha_f \nabla p + \alpha_f \nabla \cdot \boldsymbol{\tau}_f - \mathbf{K}_{sl}(\mathbf{u} - \mathbf{v}) + \alpha_f \rho_f \mathbf{g} \tag{2}$$

where the first term at the right-hand side represents the pressure gradient, $\boldsymbol{\tau}_f$ the deviatoric stress tensor for Newtonian fluids, $\mathbf{K}_{sl}$ is the volumetric-average particle-fluid implicit momentum source force term, and $\mathbf{g}$ is the gravitational acceleration force term. The implicit momentum source term can be expressed as [13]:

$$K_{\mathrm{sl}} = \frac{\alpha_f \cdot \sum_i |\mathbf{F_d}|}{V_{\mathrm{cell}} |\mathbf{u}_f - \mathbf{u}_p|} \tag{3}$$

where i is the number of particles in the CFD cell, V_{cell} is the cell volume, and $\mathbf{F}_d$ are contributions from the particles (drag, lift, virtual mass, pressure gradient, and viscous forces.) [16]. The Gidaspow correlation [17]. was used to model the drag force. The Newtonian stress tensor can be expressed as [16]:

$$\boldsymbol{\tau}_f = -\mu_f \left(\nabla \mathbf{u}_f + (\nabla \mathbf{u}_f)^T\right) + \left(\frac{2}{3}\mu_f - k\right)(\nabla \cdot \mathbf{u}_f)\mathbf{I} \tag{4}$$

where μ_f and k are dynamic and the dilatational viscosities of the fluid and $\mathbf{I}$ is the identity tensor. The energy equation for the gas phase is given by Equation (5) [18, 19]:

$$\frac{\partial(\alpha_f \rho_f E)}{\partial t} + \nabla \cdot \alpha_f \rho_f \mathbf{u}_f E = -\nabla \cdot \alpha_f p \mathbf{u}_f - \alpha_f \frac{\lambda}{c_p} \nabla \cdot e + S_{\mathrm{q}} \tag{5}$$

where E is the total energy (sum of internal energy e and kinetic energy E_k), λ is the effective thermal conductivity accounting for the particle presence [19, 20] and c_p is the specific heat capacity of the gas, calculated using the polynomial approximation with coefficients from the JANAF tables [21]. The heat source term S_q includes contributions from convection and radiation:

$$S_{\mathrm{q}} = Q_{\mathrm{conv}} + Q_{\mathrm{rad}} \tag{6}$$

The convective heat transfer is given by [22]:

$$Q_{\mathrm{conv}} = hA_p(T_f - T_p) \tag{7}$$

where A_p is the particle surface area, T_f and T_p are the fluid and particle temperatures, respectively, and h is the convective heat transfer coefficient. The convective heat transfer coefficient is defined as:

$$h = \frac{\lambda Nu}{d_p} \tag{8}$$

where d_p is the particle diameter and Nu is the Nusselt number, calculated using the correlation by Gunn [23]:

$$Nu = (7 - 10\alpha_f + 5\alpha_f^2)(1 + 0.7Re_p^{0.2}Pr^{1/3}) + (1.33 - 2.4\alpha_g + 1.2\alpha_g^2)Re_p^{0.7}Pr^{1/3} \tag{9}$$

In the equation above, Re_p is the particle Reynolds number, defined as:

$$Re_p = \frac{d_p \alpha_f \left|\mathbf{u}_f - \mathbf{u}_p\right|}{\nu_f} \tag{10}$$

where ν_f is the kinetic viscosity. The Prandtl number Pr is defined as:

$$Pr = \frac{c_p \mu_f}{k} \tag{11}$$

with k being thermal conductivity. The P1 model for CFD-DEM from [24] was used to calculate the radiative heat flux due to its numerical efficiency and its mathematical formulation is given as follows:

$$Q_{\mathrm{rad}} = G\nabla\Gamma - \nabla(\Gamma G) \tag{12}$$

In the Equation (12), the radiative diffusion Γ can be calculated according to:

$$\Gamma = \frac{1}{3\kappa + \sigma_{\text{eff}}} \tag{13}$$

where κ is the effective (combined) absorption coefficient from the fluid and particles ($\kappa = \kappa_f + \kappa_p$) and σ_{eff} is the effective scattering coefficient, given by:

$$\sigma_{\text{eff}} = 3(1 - \alpha_p)\varsigma_f + \sigma_p(3 - A_1) \tag{14}$$

where the term ς_f is the artificial scattering coefficient for the fluid phase, introduced to reduce the difference in radiative diffusion between the particle-filled and the particle-empty cells, σ_p is the scattering coefficient and A_1 is the phase function coefficient. The incident radiation intensity G is calculated using the formulation:

$$\nabla \cdot (\Gamma \nabla G) - \kappa G = -4e_f \sigma T_f^4 - E \tag{15}$$

where the term $4e_f \sigma T_f^4$ is the intensity emitted by the fluid, and E is the emission contribution of the particles [24]. The term e_f is the fluid emission coefficient, σ is the Stefan-Boltzmann constant. Species conservation is modeled using following expression [15]:

$$\frac{\partial(\rho_f \alpha_f Y_i)}{\partial t} + \nabla \cdot \alpha_f \rho_f \mathbf{u}_f Y_i = \nabla \cdot \alpha_f \rho_f D_f \nabla Y_i + S_{Y_i} \tag{16}$$

where Y_i is the mass fraction of the species i and S_{Y_i} is the source term representing mass generation or consumption of species i. The Schmidt number Sc is defined in relation to diffusivity D_f as:

$$\text{Sc} \equiv \frac{\mu_f}{\rho_f D_f} \tag{17}$$

The void fraction model for the particle representation from DEM to the CFD used the divided model from CFDEMcoupling [16, 25]. In the divided scheme, each particle's volume is discretized into 29 equal, non-overlapping sub-regions. The solid volume fraction within a single CFD cell is then calculated by summing the volumes of these sub-regions whose centroids fall inside that cell.

2.2.2 Governing equations – Particle phase

In this study, the battery cell is modeled as a multisphere particle. The multisphere clump is composed of five stacked spheres to reproduce a typical 21700 LIB cell. Figure 4 illustrates the particle dimensions.

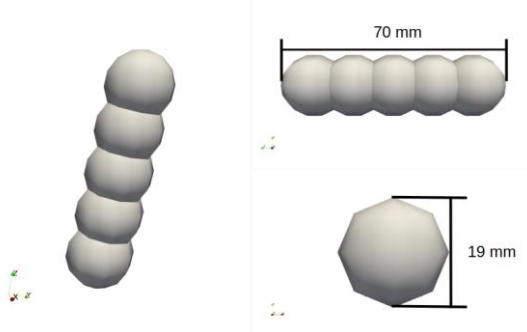

Figure 4: Multisphere clump particle battery representation

For the laboratory-scale experiment simulation, the particle is considered stationary, and movement is not solved. The battery mass change due to gas release is described by:

$$\frac{\partial m_p}{\partial t} = \sum rr_{i,g} \tag{18}$$

The reaction rate $rr_{i,g}$ is defined by Equation (19):

$$rr_{i,g} = A \exp\left(\frac{T_b}{T_{battery}}\right)\left(\frac{X_i}{X_{i,0}}\right)^n \tag{19}$$

where $rr_{i,g}$ denotes the reaction rate, A is the frequency factor, and T_{battery} and T_b are the actual battery temperature and activation temperature, respectively. X_i and $X_{i,0}$ are the current and initial gas contents, and n is the reaction order. The values of the constants used are provided in Table 1 for CO, CO_2 and C_2H_6.

Table 1: Example of the construction of one table

Species	$X_{i,0}$ [kg]	A [kg/s]	T_b [K]	n [-]
CO	6.69E-04	4.75	933	1
CO_2	0.0056	1.366	603	1
C_2H_6	13E-4	1.69	572	1

The battery temperature evolution is described as:

$$\frac{\partial T_p}{\partial t} m_p c_{p,p} = \dot{Q}_{\text{rad}} + \dot{Q}_{\text{conv}} + \dot{Q}_{\text{tr}} \tag{20}$$

The radiative heat transfer flux for a particle i can be expressed as:

$$\dot{Q}_{\text{rad},i} = \kappa_{p,i} G_i - 4E_{p,i} \tag{21}$$

where the $\kappa_{p,i}$ is the absorption coefficient, and $4E_{p,i}$ is the emission contribution, proportional to T_p^4 and the projected area [24]. The heat transfer by convection is analogous to Equation (7). The enthalpy release from the thermal runaway per particle is modeled as [26]:

$$H_{tr} = m_p c_p (T_{max} - T_{tr}) \tag{22}$$

where $T_{\max}$ is the maximum temperature reached during thermal runaway and T_{tr} is the temperature at which thermal runaway begins. Table 2 lists the parameters values used in Equation (22), which were derived from the experiments.

Table 2: Parameters for the thermal runaway modeling

Variable	Value	Unit
m_{cell}	68.6	g
m_p	13.7	g
T_{max}	786	K
T_{tr}	504	K
c_p	$907.52\,T_p + 2.97$ [27]	$\text{J}/(\text{kg}\cdot\text{K})$

2.2.1 Simulation boundary conditions

The geometry of the present study case in Figure 5 below.

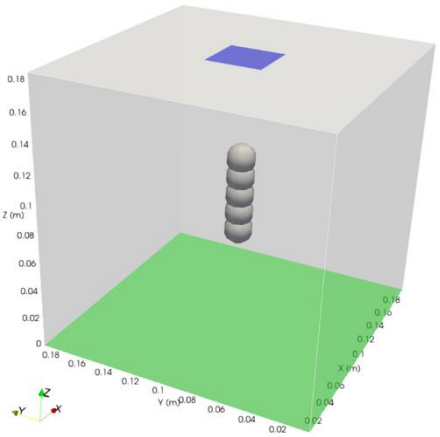

Figure 5: Simulation geometry showing the inlet (bottom green surface), outlet (upper blue surface), walls (gray surface) and a multisphere particle at the center

As seen in Figure 5, a single multisphere clump is placed in the center of the cube, which represents the steel box from the experiment with dimensions adapted to 0.185 m x 0.185 m x 0.185 m. Nitrogen gas enters from the inlet surface (bottom green Figure 5) at a velocity of U_{inlet} = 0.01130 m/s, aligned with the clump longitudinal axis. The outlet was set directly over the battery (upper blue surface in Figure 5) and was used to sample the volume fraction of the gas escaping the domain. The simulation was set to run for the same duration as the experiment, with a total time of 1800 seconds. This time covers the battery heating up to the thermal runaway temperature and subsequently cooling after the thermal energy release. The temperature of the walls and the gas inlet were set to follow a uniform data table based on the experimental data, varying from T_0 = 298 K at the time zero, up to T_f = 573 K at 1675 s. The initial temperature of the battery clump was set to $T_0^{battery} = 298\,K$.

3 RESULTS AND DISCUSSION

The results from the thermal runaway model simulation were compared to the experimental data to evaluate the model. Figure 6 illustrates the results for the chemical species volume fraction.

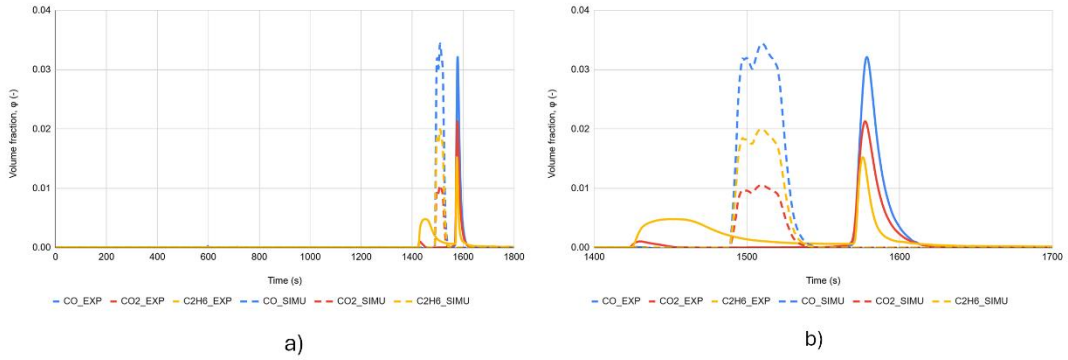

Figure 6: Comparison of experimental and simulated chemical species volume fractions. (a) shows the full experiment duration, while (b) provides a zoomed-in of the thermal runaway.

As can be seen in Figure 6 (a), the total time is 1800 s, but the thermal runaway happens in a short interval of approximately 20 s as seen in (b). The time displacement between the experimental and simulation data is attributed to model sensitivity and the lag in gas detection by the gas analyzer. The species volume fraction also presented a difference in magnitude, but this is acceptable since homogeneous gas-gas reactions were not considered due to the N_2 atmosphere. This omission means that gas species like C_2H_6 that could react to form additional CO_2 were not accounted for. Overall, the model reproduced the detected chemical species from the thermal runaway with a reasonable degree of accuracy. Figure 7 shows a comparison of experimental and simulated battery temperature.

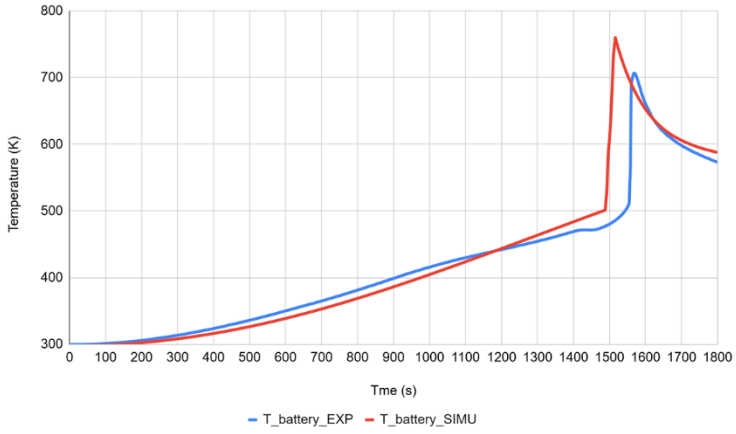

Figure 7: Comparison of simulated and experimental battery temperature.

The battery temperature plot illustrates the transition from room temperature to thermal runaway, followed by cooling after the thermal energy release. The time interval from 0 to approximately 1450 s corresponds to the initial heating stage, before the battery's safety valve is activated. When the particles reach $T_{tr} = 504\,\mathrm{K}$ and the heating rate exceeds 1 K/s ($dT/dt > 1$), thermal runaway occurs. This is observed at 1489 s in the simulation and 1550 s in the experiment, resulting in a rapid temperature increase. Afterward, the system cools down via convection with the shielding gas until it reaches the furnace set point temperature. Figure 8

illustrates battery temperature and species volume fraction (CO, CO_2, and C_2H_6) during thermal runaway.

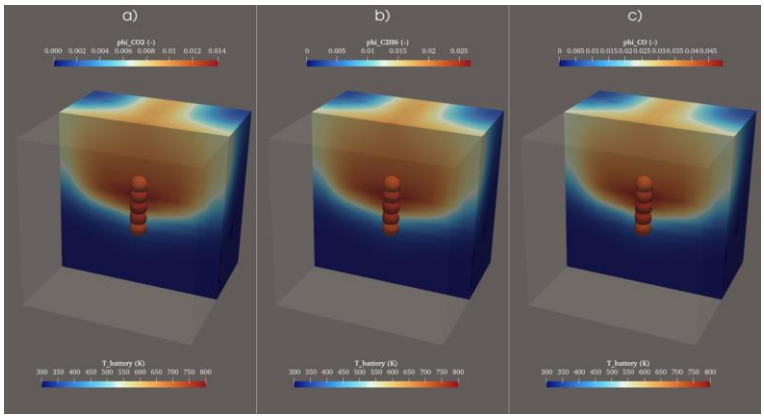

Figure 8: Cross-section of the simulation domain showing chemical species volume fraction (a-CO_2, b-C_2H_6 and c-CO) and particle temperature during the thermal runway.

As shown in Figure 8, the domain is partially filled with gas originating from particle reactions. The gases are generated from the surfaces of each particle, spread toward the domain walls, and are subsequently directed toward the upper outlet by the inlet gas velocity. The species concentration is significantly higher near the particles, reducing as it moves away from each sphere due to mixing with the incoming N_2 from the inlet. The particle temperature at this moment is at its peak, exceeding 700 K, which indicates that the reaction is almost complete.

4 CONCLUSION

The physical and chemical behavior of the thermal deactivation phenomenon was replicated through small-scale laboratory experiments, and the results were used to set the initial temperature conditions and species production rates for the CFD-DEM simulation. Using established equations and experimental data, thermal runaway energy release and kinetic reaction expressions were implemented. This initial implementation provided a preliminary validation of the core thermal and mass loss mechanisms, offering insight into the simulation domain's behavior under extreme conditions. The next steps involve completing the implementation of the species release and varying the State of Charge (SOC) modeling. In the future, this numerical model will be used to design and study thermal deactivation process in industrial-scale applications.

REFERENCES

[1] Wang, Y., An, N., Wen, L., Wang, L., Jiang, X., Hou, F., Yin, Y., Liang, J.: Recent progress on the recycling technology of Li-ion batteries. Journal of Energy Chemistry 55, 391–419 (2021) https://doi.org/10.1016/j.jechem.2020.05.008.

[2] Li, P., Luo, S., Zhang, L., Liu, Q., Wang, Y., Lin, Y., Xu, C., Guo, J., Cheali, P., Xia, X.: Progress, challenges, and prospects of spent lithium-ion batteries recycling: A review. Journal of Energy Chemistry 89, 144–171 (2024) https://doi.org/10.1016/j.jechem.2023.10.012.

[3] Jung, J., Sui, P.-C., Zhang, J.: Hydrometallurgical Recycling of Lithium-Ion Battery Materials. CRC Press (2023).
[4] Consortium, B.P., et al.: Battery passport content guidance. Achieving compliance with the EU Battery Regulation and Increasing Sustainability and Circularity. Version 1 (2023). https://eur-lex.europa.eu/legal-content/EN/TXT/PDF/?uri=CELEX:32023R1542, Last accessed: 10-09-2025.
[5] Lin, J., Zhang, X., Fan, E., Chen, R., Wu, F., Li, L.: Carbon neutrality strategies for sustainable batteries: from structure, recycling, and properties to applications. Energy & Environmental Science 16(3), 745–791 (2023) https://doi.org/10.1039/ D2EE03257K.
[6] Yu, J., He, Y., Ge, Z., Li, H., Xie, W., Wang, S.: A promising physical method for recovery of LiCoO2 and graphite from spent lithium-ion batteries: Grinding flotation. Separation and Purification Technology 190, 45–52 (2018) https://doi. org/10.1016/j.seppur.2017.08.049.
[7] Rothermel, S., Evertz, M., Kasnatscheew, J., Qi, X., Gr¨utzke, M., Winter, M., Nowak, S.: Graphite Recycling from Spent Lithium-Ion Batteries. ChemSusChem 9(24), 3473–3484 (2016) https://doi.org/10.1002/cssc.201601062
[8] Rothermel, S., Evertz, M., Kasnatscheew, J., Qi, X., Gr¨utzke, M., Winter, M., Nowak, S.: Graphite Recycling from Spent Lithium-Ion Batteries. ChemSusChem 9(24), 3473–3484 (2016) https://doi.org/10.1002/cssc.201601062
[9] Yang, Y., Huang, G., Xu, S., He, Y., Liu, X.: Thermal treatment process for the recovery of valuable metals from spent lithium-ion batteries. Hydrometallurgy 165, 390–396 (2016) https://doi.org/10.1016/j.hydromet.2015.09.025.
[10] Rosen, M.A., Farsi, A.: Battery Technology. Elsevier Science & Technology, London, United Kingdom (2023).
[11] Weller, H.G., Tabor, G., Jasak, H., Fureby, C.: A tensorial approach to computational continuum mechanics using object-oriented techniques. Computers in Physics 12(6), 620–631 (1998) https://doi.org/10.1063/1.168744.
[12] Kloss, C., Goniva, C., König, A., Amberger, S., Pirker, S.: Models, algorithms and validation for opensource DEM and CFD-DEM. Progress in Computational Fluid Dynamics 12, 140–152 (2012) https://doi.org/10.1504/PCFD.2012.047457.
[13] Goniva, C., Kloss, C., Deen, N.G., Kuipers, J.A.M., Pirker, S.: Influence of rolling friction on single spout fluidized bed simulation. Particuology 10(5), 582–591 (2012) https://doi.org/10.1016/j.partic.2012.05.002.
[14] Tao, H., Tao, J.: Quantitative analysis of piping erosion micro-mechanisms with coupled CFD and DEM method. Acta Geotechnica 12 (2017) https://doi.org/ 10.1007/s11440-016-0516-y.
[15] Kim, J., Mallarapu, A., Finegan, D.P., Santhanagopalan, S.: Modeling cell venting and gas-phase reactions in 18650 lithium ion batteries during thermal runaway. Journal of Power Sources 489, 229496 (2021) https://doi.org/10.1016/j.jpowsour. 2021.229496
[16] Norourzi, H., Zarghami, R., Sotudeh-Gharebagh, R., Mostoufi, N.: Coupled CFDDEM Modeling: Formulation, Implementation and Application to Multiphase Flows. John Wiley & Sons (2016).
[17] Gidaspow, D.: Multiphase Flow and Fluidization: Continuum and Kinetic Theory Descriptions. Academic Press (1994).
[18] Kinaci, M.E., Lichtenegger, T., Schneiderbauer, S.: A CFD-DEM model for the simulation

of direct reduction of iron-ore in fluidized beds. Chemical Engineering Science 227, 115858 (2020) https://doi.org/10.1016/j.ces.2020.115858.
[19] Lichtenegger, T., Pirker, S.: Fast long-term simulations of hot, reacting, moving particle beds with a melting zone. Chemical Engineering Science 283, 119402 (2024) https://doi.org/10.1016/j.ces.2023.119402.
[20] Syamlal, M., Gidaspow, D.: Hydrodynamics of fluidization: Prediction of wall to bed heat transfer coefficients. AIChE Journal 31(1), 127–135 (1985) https: //doi.org/10.1002/aic.690310115.
[21] Burcat, A., Ruscic, B.: Third millenium ideal gas and condensed phase thermochemical database for combustion (with update from active thermochemical tables). Technical Report ANL-05/20, Argonne National Laboratory (ANL) (2005). https://doi.org/10.2172/925269.
[22] Li, J., Mason, D.J.: A computational investigation of transient heat transfer in pneumatic transport of granular particles. Powder Technology 112(3), 273–282 (2000) https://doi.org/10.1016/S0032-5910(00)00302-8.
[23] Gunn, D.J.: Transfer of heat or mass to particles in fixed and fluidised beds. International Journal of Heat and Mass Transfer 21(4), 467–476 (1978).
[24] Mačak, J.: CFD-DEM simulation of high-temperature processes. Graz. Book Title: CFD-DEM simulation of high-temperature processes (2023). https://dx. doi.org/10.3217/0qh2z-3qy75
[25] CFDEMcoupling documentation: Divided void fraction command. https://www. cfdem.com/media/CFDEM/docu/voidFractionModel dividedVoidFraction.html Accessed 2025-09-09.
[26] Jhu, C.-Y., Wang, Y.-W., Shu, C.-M., Chang, J.-C., Wu, H.-C.: Thermal explosion hazards on 18650 lithium ion batteries with a VSP2 adiabatic calorimeter. Journal of Hazardous Materials 192(1), 99–107 (2011) https://doi.org/10.1016/j.jhazmat. 2011.04.097.
[27] Yu, H., Zhang, H., Shi, J., Liu, S., Yi, Z., Xu, S., Wang, X.: Thermal parameters of cylindrical power batteries: Quasi-steady state heat guarding measurement and thermal management strategies. Applied Thermal Engineering 231, 120959 (2023) https://doi.org/10.1016/j.applthermaleng.2023.120959.